ADVANCED SCIENCE
Open Access
www.advancedscience.com

Modulation of Contact Resistance of Dual-Gated MoS_2 FETs Using Fermi-Level Pinning-Free Antimony Semi-Metal Contacts

Tien Dat Ngo, Tuyen Huynh, Hanggyo Jung, Fida Ali, Jongwook Jeon, Min Sup Choi, and Won Jong Yoo**

Achieving low contact resistance (R_C) is one of the major challenges in producing 2D FETs for future CMOS technology applications. In this work, the electrical characteristics for semimetal (Sb) and normal metal (Ti) contacted MoS_2 devices are systematically analyzed as a function of top and bottom gate-voltages (V_{TG} and V_{BG}). The semimetal contacts not only significantly reduce R_C but also induce a strong dependence of R_C on V_{TG}, in sharp contrast to Ti contacts that only modulate R_C by varying V_{BG}. The anomalous behavior is attributed to the strongly modulated pseudo-junction resistance (R_{jun}) by V_{TG}, resulting from weak Fermi level pinning (FLP) of Sb contacts. In contrast, the resistances under both metallic contacts remain unchanged by V_{TG} as metal screens the electric field from the applied V_{TG}. Technology computer aided design simulations further confirm the contribution of V_{TG} to R_{jun}, which improves overall R_C of Sb-contacted MoS_2 devices. Consequently, the Sb contact has a distinctive merit in dual-gated (DG) device structure, as it greatly reduces R_C and enables effective gate control by both V_{BG} and V_{TG}. The results offer new insight into the development of DG 2D FETs with enhanced contact properties realized by using semimetals.

1. Introduction

Transition-metal dichalcogenides (TMDs) are a promising candidate for semiconducting channel materials that are expected to be useful in future CMOS devices due to their bodies that are atomically thin and free of dangling bonds, thus enabling efficient electrostatic control at very low voltages. One of the most studied materials among this TMD family is MoS_2. In recent years, there have been many efforts aiming to further improve the performance of 2D-based FETs, e.g., contact engineering.[1–7] However, the notoriously high contact resistance (R_C) in MoS_2 FETs hinders the realization of high-performance electronic devices. Several techniques have recently been reported to improve R_C by utilizing semimetals as contact metals for MoS_2 FETs, which can substantially suppress the metal-induced gap states (MIGS).[8–15]

Nonetheless, most studies have investigated the contact properties in a single-gated (SG) architecture rather than a dual-gated (DG) architecture. Conventional SG planar devices encounter a severe challenge such as poor electrostatic controllability due to their short channel effects, which hinders further scaling of the devices. By contrast, the DG can enable more efficient control of the channel resistance of 2D layered material-based FET devices, and it can also be used for high-performance and variously designed gate-integrated CMOS circuits.[16–20] Several studies have used multi-bridge channel FETs, which are analogous to a DG structure, to achieve excellent electrostatic controllability and power/area efficiency.[21–24] Moreover, a research group has recently explored DG MoS_2 FETs with a channel length of 25 nm, which show a comparable performance to state-of-the-art Si technology.[25] Thus, the DG architectures of high-performance 2D FETs need to be developed to ensure a long-term continuity of Moore's Law scaling.

Meanwhile, some studies have shown that overall R_C is independent of top-gate voltage (V_{TG}) in DG FETs, because the V_{TG}-induced electric field can be screened by metal electrodes, resulting in unchanged intrinsic resistance under the contacts (R_{ci}).[19,20] It should be noted that the normal metals used in these studies induce strong Fermi level pinning (FLP) at the

T. D. Ngo, T. Huynh, W. J. Yoo
SKKU Advanced Institute of Nano Technology
Sungkyunkwan University
Suwon, Gyeonggi-do 16419, Republic of Korea
E-mail: yoowj@skku.edu
H. Jung, J. Jeon
Department of Electrical and Electronics Engineering
Konkuk University
Seoul 05029, Republic of Korea
F. Ali
Department of Electronics and Nanoengineering
Aalto University
P.O. Box 13500, Espoo FI-00076, Finland
M. S. Choi
Department of Materials Science and Engineering
Chungnam National University
Daejeon 34134, Republic of Korea
E-mail: goodcms@cnu.ac.kr

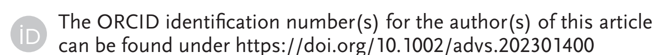
The ORCID identification number(s) for the author(s) of this article can be found under https://doi.org/10.1002/advs.202301400

© 2023 The Authors. Advanced Science published by Wiley-VCH GmbH. This is an open access article under the terms of the Creative Commons Attribution License, which permits use, distribution and reproduction in any medium, provided the original work is properly cited.

DOI: 10.1002/advs.202301400

21983844, 0, Downloaded from https://onlinelibrary.wiley.com/doi/10.1002/advs.202301400 by Sungkyunkwan University, Wiley Online Library on [26/06/2023]. See the Terms and Conditions (https://onlinelibrary.wiley.com/terms-and-conditions) on Wiley Online Library for rules of use; OA articles are governed by the applicable Creative Commons License

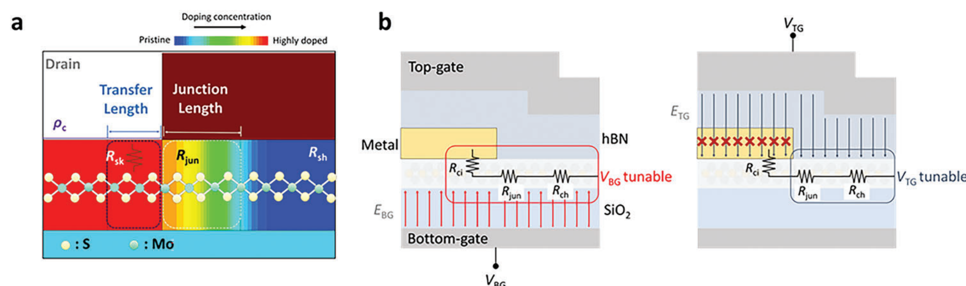

Figure 1. a) Schematic of a MoS_2 FET at the drain contact side showing doping concentration profile at the contact and channel regions. b) Schematic of a DG MoS_2 FET showing R_C components that consist of R_{ci} and R_{jun}. The E_{TG} is screened by the metal electrode, while the E_{BG} can tune all the R_C components.

metal–semiconductor (MS) interface; therefore, the lateral junction resistances near the contacts are also unchanged by V_{TG}.[26–28] Recently, to reveal such FLP-dependent contact behaviors, the classical model on contact interface between metal and semiconductor involving specific contact resistivity (ρ_c) and sheet resistance under the metal contact (R_{sk}) has been further developed by adding pseudo-lateral junction resistance (R_{jun}) components to the total R_C in 2D-based FETs.[29–31] Venica et al. first proposed the use of the R_{jun} component to explain the gate-tunable R_C.[30] Moreover, Ber et al. proposed a unique approach to specifically probe the R_{jun} component by 4-point probe (4PP) measurements, which also helps to extract various metallic contact-related resistance components.[29] Meanwhile, Kong et al. performed a DFT band calculation that showed clear differences in the contact resistance components between FLP-dominant and FLP-free metal contact platforms.[32]

In this work, we used a semimetal (antimony, Sb) as a top surface electrode and hBN as a top-gate (TG) dielectric for the purpose of realizing an FLP-free MS interface in DG MoS_2 FETs. Ohmic contact is realized with the Sb contact by suppressing MIGS at the Sb and MoS_2 interface.[8,9] We performed systematic 4PP measurements to extract R_C as a function of bottom-gate voltage (V_{BG}) and V_{TG}. Interestingly, our Sb-contacted devices showed that R_C is modulated sensitively by both V_{TG} and V_{BG}, which is in sharp contrast with Ti-contacted devices showing R_C modulation only by V_{BG}. To further understand this anomalous contact behavior of Sb-contacted devices, we extracted R_{jun} and R_{ci} as functions of DG voltages.[29] The results showed that R_{jun} is significantly modulated by both V_{TG} and V_{BG} while R_{ci} is modulated only by V_{BG}. By contrast, R_{jun} and R_{ci} of Ti-contacted devices are weakly tuned by V_{TG} due to strong FLP. This work suggests that the FLP-free semimetal contacts can be used to efficiently modulate R_C in DG MoS_2 FETs by applying both V_{BG} and V_{TG}. Technology computer-aided design (TCAD) simulations further confirm the role of V_{TG} in improving R_{jun} toward high-performance Sb-contacted DG MoS_2 devices.

2. Results and Discussion

Figure 1a shows a schematic of MoS_2 FET with R_C components at the MS contact. To systematically investigate the impacts of V_{BG} and V_{TG} on overall R_C, we decompose R_C into R_{ci} and R_{jun}.[29–31] R_{ci} is the resistance component under the electrode that consists of ρ_c and R_{sk}. Here, when using our FLP-free devices, the gate-tunable R_{jun} is mostly attributable to the difference in doping concentration between MoS_2 under the contact and at the channel area that originates from heavy n-type doping in MoS_2 by semimetal Sb, forming a gate-tunable n$^+$-n junction. Figure 1b represents a schematic of a DG MoS_2 FET showing the impact of V_{TG} and V_{BG} on contact resistance components of the device. As Ber et al. reported, R_{ci} is weakly dependent on V_{BG} due to FLP and high doping concentration under the contact.[29] Moreover, R_{ci} is supposed to be independent of V_{TG}, as the electric field induced by V_{TG} (E_{TG} as indicated in the diagram) is screened by the covered metal electrodes. In contrast, R_{jun} is found to be V_{BG} tunable due to the modulation of lateral junction potential.[29–31] Furthermore, R_{jun} is supposed to be strongly modulated by V_{TG} unlike R_{ci} as it is not covered by the metal electrode.[29–31] Thus, we believe that overall R_C could be affected by applying V_{BG} and V_{TG} simultaneously in the DG structure considering such strong modulation of R_{jun}.

To investigate the impact of V_{TG} on R_C, we fabricated DG MoS_2 FETs with Sb (and DG MoS_2 FETs with Ti as a reference) electrodes on a global bottom-gate (BG) silicon substrate capped with 285 nm SiO_2 (To ensure the screening effect of metal electrode against V_{TG}, total thickness of ≈25 nm is used).[33] The TG of the device is formed by an exfoliated hBN flake (≈50 nm) with a TG electrode of Ti/Au (5/70 nm). The detailed fabrication process is described in the Experimental Section. The Raman spectra and atomic force microscopic (AFM) images of MoS_2 and hBN are shown in Figure S1 (Supporting Information). The dry-transferred hBN possibly results in the formation of air gap at the metal-MoS_2 junction where the top hBN is not fully contacted with MoS_2 channel. However, if we consider the air gap as a dielectric layer with a dielectric constant of 1, MoS_2 area at the gap is still electrostatically tunable by V_{TG}. In this sense, Zhang et al. have reported that 2D semiconductors can be electrostatically doped by applying gate-voltages despite the existence of air gap at the metal-2D semiconductor junction.[33] Therefore, although the existence of the air gap at metal-MoS_2 junction may affect the top-gate performance, the electrostatic modulation of R_C and R_{jun} by V_{TG} is still possible.

Figure 2a illustrates the final structure of the DG MoS_2 FET. The transfer characteristic of the DG FET with Sb contacts is depicted in Figure 2b. The device with L_{CH} = 11.5 μm achieves I_{ON} of ≈8 μA μm^{-1} at V_{DS} = 1 V with a good I_{ON}/I_{OFF} ratio of ≈10^7 without V_{TG}. The Ohmic behavior of Sb contact is evidenced by the linear output characteristic, as represented in Figure 2c. It is

 © 2023 The Authors. Advanced Science published by Wiley-VCH GmbH

21983844, 0, Downloaded from https://onlinelibrary.wiley.com/doi/10.1002/advs.202301400 by Sungkyunkwan University, Wiley Online Library on [26/06/2023]. See the Terms and Conditions (https://onlinelibrary.wiley.com/terms-and-conditions) on Wiley Online Library for rules of use; OA articles are governed by the applicable Creative Commons License

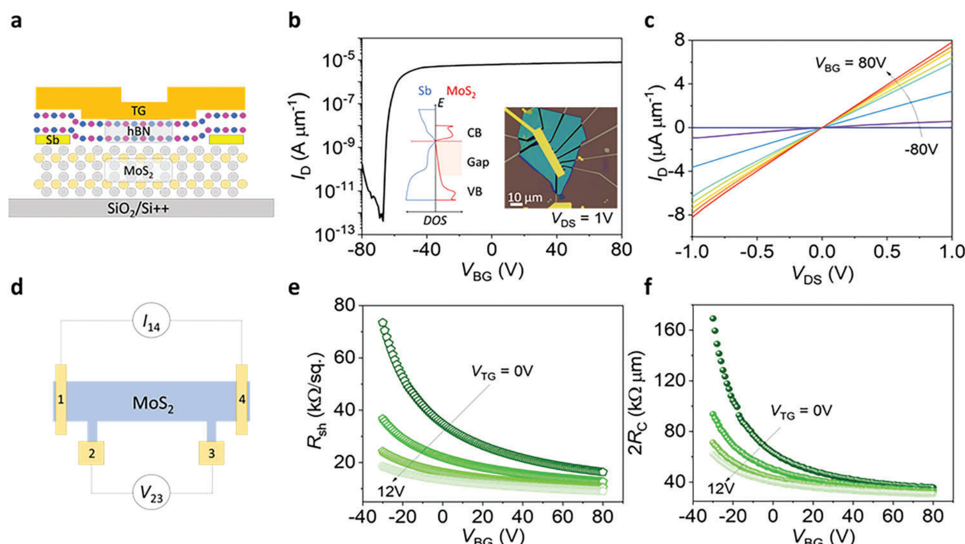

Figure 2. a) Schematic of a Sb-contacted DG MoS_2 FET. b) Transfer characteristics of the FET with $V_{DS} = 1$ V and $V_{TG} = 0$ V. The insets show an optical image of the device and a band structure showing the DOS of Sb and MoS_2. c) Output characteristic of the FET by varying $V_{BG} = -80$ to 80 V ($V_{TG} =$ 0 V). d) Schematic of a 4PP measurement configuration of the FET. e) R_{sh} and f) $2R_C$ as a function of V_{BG} at different V_{TG} obtained from the FET.

noted that the linear behavior is also obtained without gating the contact area by sweeping V_{TG} from −12 to 12 V at $V_{BG} = 0$ V (Figure S2, Supporting Information), which shows the superiority of Sb semimetal over normal metals. The mobilities and hysteresis behavior of Sb-contacted DG MoS_2 FETs extracted from the transfer curves with V_{TG} and V_{BG} are shown in Figures S3 and S4 (Supporting Information). As a reference, the transfer and output characteristics of Ti-contacted DG MoS_2 FET are shown in Figure S5 (Supporting Information). Unlike Sb contacts, asymmetric output characteristics are observed with both V_{TG} and V_{BG} in Ti-contacted device. We further demonstrate the distinctive V_{TG}-dependent transfer characteristics of the Sb-contacted device compared to the Ti-contacted device as shown in Figure S6 (Supporting Information). Both devices show a similar improvement in on-state current when V_{TG} increases; however, the threshold voltage (V_{th}) of the Sb-contacted device is strongly shifted to negative V_{TG}, while the Ti-contacted device revealed a slight V_{th} shift. The origin of this phenomenon can be explained by the different V_{TG}-dependent R_C between both devices as discussed in **Figure 3**.

To evaluate the FLP behavior of the devices, we further conducted temperature-dependent measurements of the transfer characteristics to extract Schottky barrier height (SBH), as depicted in Figure S7 (Supporting Information). The Sb-contacted device shows a negligible SBH (≈0 meV), while the Ti-contacted device shows a relatively high SBH (≈200 meV) despite the fact that both the metals have similar work functions (4.4 eV for Sb and 4.33 eV for Ti).[8,34] The FLP behavior of both devices can be understood by band alignment, as depicted in Figure S7d,e (Supporting Information). The negligible SBH of the Sb-contacted device is consistent with intrinsic band alignment showing FLP-free contact for the 2D MoS_2 FET. This FLP-free behavior is consistent with the DFT calculation performed by Chou et al., which shows suppressed MIGS (inset of Figure 2b).[9] Ti is supposed to have Ohmic contact with 2D MoS_2 (≈0 meV) according to the iso-

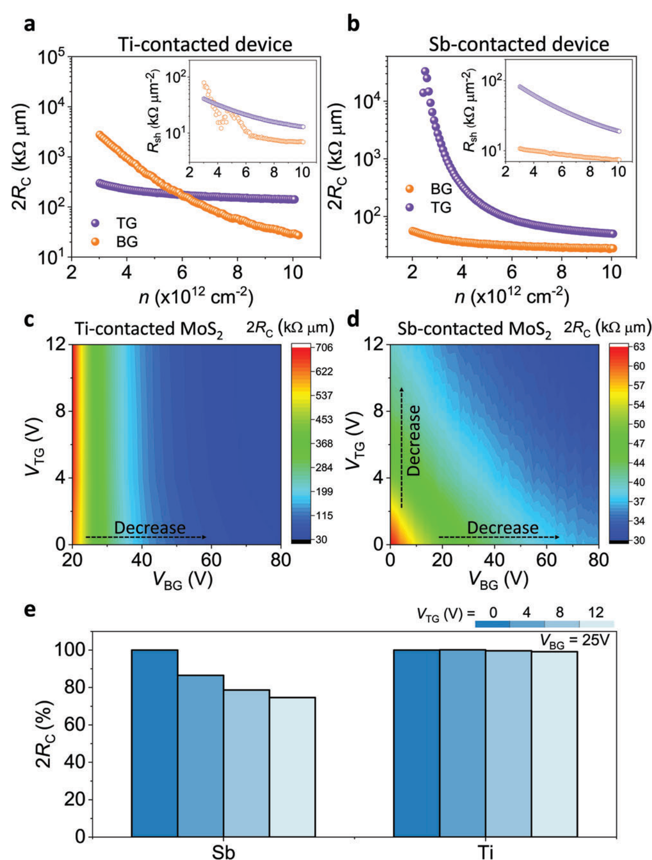

Figure 3. $2R_C$ of a) Ti- and b) Sb-contacted devices measured by 4PP measurements with separate TG and BG biases. The inset shows R_{sh} as a function of carrier densities. $2R_C$ map as a function of V_{TG} and V_{BG} for c) Ti- and d) Sb-contacted DG MoS_2 FETs. e) Modulated percentages of $2R_C$ as a function of V_{TG} at a fixed $V_{BG} = 25$ V.

© 2023 The Authors. Advanced Science published by Wiley-VCH GmbH

lated band structure, but the actual SBH is ≈200 meV, implying a strong FLP.

Figure 2d illustrates the device configuration used in the 4PP measurements to extract the R_C of the DG MoS_2 devices. A fixed current ($I_{14} = 0.33\ \mu A \cdot \mu m^{-1}$) is applied between electrodes 1 and 4, and the voltage is probed at each electrode. By measuring the voltage drop between electrodes 2 and 3 (ΔV_{23}), sheet resistance (R_{sh}) can be calculated by:

$$R_{sh} = \frac{\Delta V_{23}}{I_{14} \times L_{23}} \tag{1}$$

Moreover, R_C can be calculated by:

$$2R_C = \frac{\Delta V_{14}}{I_{14}} - \frac{\Delta V_{23} \times L_{14}}{I_{14} \times L_{23}} \tag{2}$$

where $L_{14} = 11.5\ \mu m$ and $L_{23} = 5.8\ \mu m$ are the distances between electrodes 1–4 and 2–3, respectively. Figure 2e exhibits R_{sh} as a function of V_{BG} that shows strong gate-tunability with V_{BG} and V_{TG}, since R_{ch} is gate-tunable, as depicted in Figure 1b. We observed a noticeable reduction in R_{sh} from 16 to 9 kΩ per square when V_{TG} increases from 0 to 12 V, which is a typical behavior for n-type semiconductors. This observation is consistent with previous results for DG 2D FETs.[17,19,20] Figure 2f presents the R_C as a function of V_{TG} derived from Equation (2). Interestingly, we noticed a considerable improvement in R_C (63 to 40 kΩ μm at V_{BG} = 0 V) with the increase in V_{TG} from 0 to 12 V. This behavior can be reproduced in other separately prepared devices as shown in Figure S8 and S9. In all devices, R_C of Sb-contacted device strongly depends on V_{TG}. The strong V_{TG}-tunability of overall R_C in Sb-contacted DG MoS_2 FETs is in contrast to the results obtained from the previous studies with normal metal contacts.[19,20] The almost unchanged R_C regardless of V_{TG} in these studies can be attributed to the screening effect of E_{TG} by top-contact metals and strong FLP.[19,20]

For a comparison, we also performed the same 4PP measurement with Ti-contacted DG MoS_2 FETs. The R_{sh} and R_C values measured at different V_{TG} and V_{BG} of the devices are presented in Figure S10 (Supporting Information). The $2R_C$ and R_{sh} measured with separate V_{TG} and V_{BG} for both the Sb- and Ti-contacted devices are represented in Figure 3a,b. For a fair comparison, we plotted the R_{sh} and R_C as a function of carrier concentration, which is extracted by the equation, $n = q^{-1} C_{TG}(V_{TG} - V_{th})$, where q is the electron charge and C_{TG} is the TG capacitance (= 1.23×10^{-7} F cm^{-2} for a 50 nm thick top hBN gate dielectric). The R_{sh} of both devices demonstrate a similar trend and values; however, R_C tunability is clearly different. The R_C of the Sb-contacted device is strongly V_{TG} tunable, while a weak V_{TG}-dependent R_C is obtained with the Ti-contacted device. Thus, we think that the difference in transfer characteristics of both the devices (different V_{th} shift with V_{TG} in Figure S6, Supporting Information) is mostly originated from the strong V_{TG}-dependent R_C of the Sb-contacted device compared to the weak V_{TG}-dependent R_C of the Ti-based device, as shown in Figure 3a,b.

Based on Figure 2f and Figure S10b (Supporting Information), we reproduced R_C map to visualize the different trends in R_C between Ti and Sb contacts depending on V_{TG} and V_{BG}, as depicted in Figure 3c,d. For the Ti-contacted device, R_C is modulated by V_{BG}, while it remains unchanged by V_{TG}, as shown in the color gradient of the map, indicating that R_C is dominated by V_{BG} (Figure 3a). This phenomenon has also been observed in previous studies with the same device architecture and normal metals.[19,20] By contrast, a distinctive behavior is observed with the Sb-contacted device; R_C varies largely by both V_{BG} and V_{TG}, as can be seen from the continuous variation of color gradient in Figure 3d. Figure 3e presents such $2R_C$ change in percentage as a function of V_{TG}, showing a roughly 30% improvement when V_{TG} increases from 0 to 12 V with Sb contacts. However, Ti contact reduces $2R_C$ by merely ≈1% with the same V_{TG} condition.

To elucidate the origin of the anomalous behavior of Sb-contacted device, we utilized the method proposed by Ber et al.[29] to extract R_{jun} and R_{ci} based on the $2R_C$ value obtained by 4PP measurements, thereby identifying predominant resistance components in R_C. **Figure 4**a illustrates an equivalent circuit and a corresponding band structure, including R_{jun} and R_{ci} at the MS interface.[29,30] The total contact resistance is expressed by:

$$2R_C = 2R_{ci} + R_{jun} \tag{3}$$

Here, R_{ci} is multiplied by 2 as the current passes through the source and drain electrodes. R_{jun} is found at the contact where the current is injected, thus, it is considered to have appeared only once in the above expression.[29] Next, the resistance between the current injecting electrode and the nearest voltage probing electrode (R_{12}) is expressed as:

$$R_{12} = \frac{\Delta V_{12}}{I_{14}} = R_{ci} + R_{jun} + R_{sh} L_{12} \tag{4}$$

where L_{12} (= 3.2 μm) is the distance between electrodes 1 and 2. Based on Equations (3) and (4), we extracted R_{jun} and R_{ci} using the value of $2R_C$ obtained through 4PP measurements. Figure 4b shows the calculated R_{jun} and R_{ci} values of the Sb-contacted device at V_{BG} = -30 to 80 V and V_{TG} = 0 V. It should be noted that R_{jun} is strongly dependent on V_{BG}, unlike R_{ci}. R_{jun} can mainly originate from the strong electron doping effect of semimetal to MoS_2 underneath the contact, thus resulting in the formation of $n^+ - n$ junction, where an n-type region is located at the channel side.[8,29] The contribution of SBH can be negligible in R_{jun} due to the FLP-free nature of semimetal contacts, as shown in Figure S7 (Supporting Information). Therefore, the potential barrier at the junction can be reduced when V_{BG} increases because the n-region becomes a highly doped n^+-state as a result of electrostatic doping due to weak FLP. However, the n^+-region underneath the semimetal is not significantly affected by V_{BG} due to its high electron concentration.[6,35,36]

Figure 4c shows R_{jun} of the Sb-contacted DG device as a function of V_{BG} with different V_{TG}. Interestingly, R_{jun} is highly modulated by V_{TG}, confirming that E_{TG} can modulate R_C. At high V_{TG} = 12 V, R_{jun} becomes independent of V_{BG}. This validates the fact that the electrostatic doping effect of E_{TG} significantly suppresses the potential barrier, equalizing the electron concentration of both MoS_2 under the metal contact and at the channel area. In contrast, R_{ci} is very weakly dependent on V_{TG} as shown in Figure 4d, which can be understood as the metal screening effect. Thus, the improvement in R_C by V_{TG}, as shown in Figure 2f and 3b, is mostly attributed to the reduced R_{jun}.

 © 2023 The Authors. Advanced Science published by Wiley-VCH GmbH

21983844, 0, Downloaded from https://onlinelibrary.wiley.com/doi/10.1002/advs.202301400 by Sungkyunkwan University, Wiley Online Library on [26/06/2023]. See the Terms and Conditions (https://onlinelibrary.wiley.com/terms-and-conditions) on Wiley Online Library for rules of use; OA articles are governed by the applicable Creative Commons License

21983844, 0, Downloaded from https://onlinelibrary.wiley.com/doi/10.1002/advs.202301400 by Sungkyunkwan University, Wiley Online Library on [26/06/2023]. See the Terms and Conditions (https://onlinelibrary.wiley.com/terms-and-conditions) on Wiley Online Library for rules of use; OA articles are governed by the applicable Creative Commons License

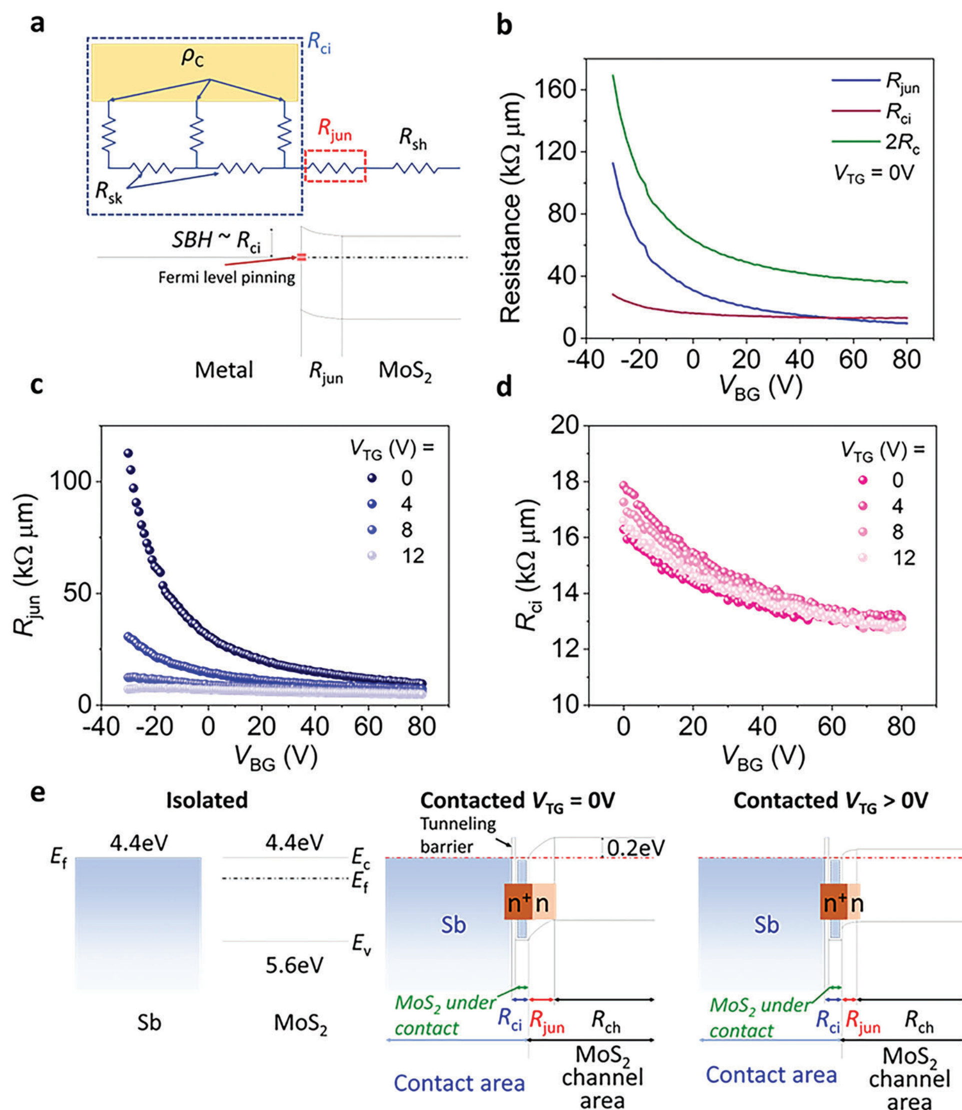

Figure 4. a) An equivalent circuit with resistance components at the MS contact and a corresponding band diagram illustrating FLP. b) R_{ci}, R_{jun}, and $2R_C$ as a function of V_{BG} at $V_{TG} = 0$ V, and c) R_{jun} and d) R_{ci} as a function of V_{BG} and V_{TG} for the Sb-contacted DG MoS_2 FET. e) Band diagrams for Sb-contacted MoS_2 illustrating how R_{jun} is modulated by V_{TG}.

The band diagram in Figure 4e describes the mechanism by which V_{TG} adjusts R_{jun}. At $V_{TG} = 0$ V, the potential barrier is formed by band alignment between MoS_2 and Sb based on their work functions. As a result, MoS_2 underneath Sb contact is strongly n-type doped, forming a n^+-n lateral junction with MoS_2 at the channel area. Therefore, the n^+-n lateral junction dominantly contributes to R_{jun}. When V_{TG} increases, the Fermi level of MoS_2 at the channel area is expected to move upward, leading to a reduced potential barrier. Moreover, the depletion width in n^+-n lateral junction decreases by equalizing the doping concentration between MoS_2 underneath the contact and at the channel area. This reduction in potential barrier and depletion width at high V_{TG} contributes to the decreased R_{jun}.

For the Ti-contacted device, the extracted R_{jun} and R_{ci} are presented in Figure S10c,d (Supporting Information). Unlike the Sb-contacted device, R_{jun} is weakly dependent on V_{TG}, presumably due to strong FLP. Since the Fermi level of MoS_2 is strongly pinned at the MIGS or defect states, it barely shifts by V_{TG}, particularly at the MS interface. Since R_{ci} is also independent of V_{TG}, R_C for the Ti-contacted device appears to be overall unchanged by V_{TG}. This interpretation is further supported by a recent work on DFT calculation, which shows tunable band alignment of MS contact with Sb contacts due to their lack of MIGS, while unnoticeable tunability is observed with normal metals.[13] Consequently, our work provides a distinctive advantage of semimetal-contacted DG device in terms of its ability to modulate R_C with V_{TG}.

Last, we verify our experimental results and mechanism by performing TCAD simulations. **Figure 5**a shows a device structure of Sb-contacted DG device used for our simulations (detailed information and parameters are described in the Experimental Section and Table S1, Supporting Information). The simulation

 © 2023 The Authors. Advanced Science published by Wiley-VCH GmbH

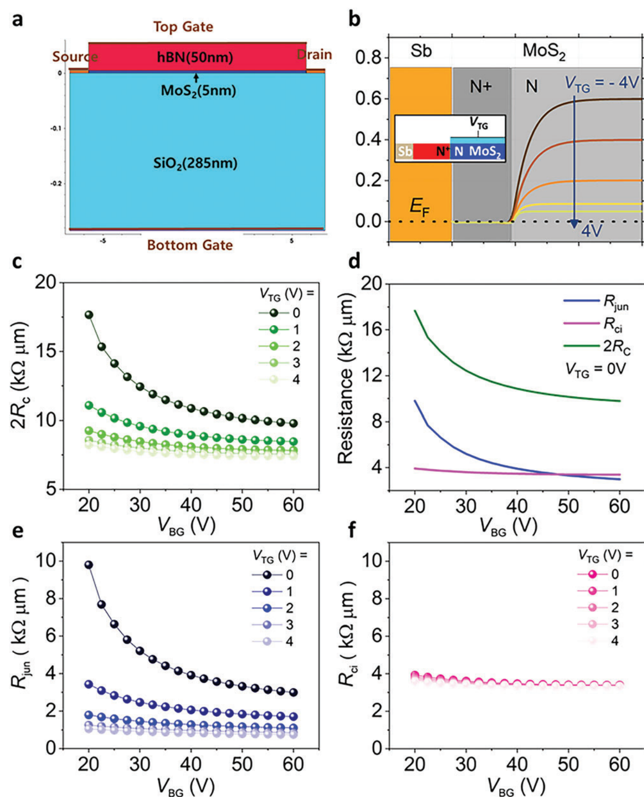

Figure 5. a) Device structure for TCAD simulations. b) Band alignment between Sb and MoS_2 with varied V_{TG}. c) Simulated $2R_C$ of Sb-contacted DG device as a function of V_{TG} and V_{BG}. d) Simulated R_{ci}, R_{jun}, and $2R_C$ as a function of V_{BG} at $V_{TG} = 0$ V. Simulated e) R_{jun} and f) R_{ci} as a function of V_{BG} and V_{TG}.

assumes that the SBH of Sb-contacted DG device to be zero due to its FLP-free nature, as confirmed by our SBH measurement in Figure S7 (Supporting Information). Furthermore, the n^+-n junction is considered at the MS junction as Sb semimetal can induce heavy n-type doping to MoS_2. As shown in Figure 5b, the potential barrier of Sb-contacted DG device significantly decreases as V_{TG} increases, which is consistent with our above postulation on strong modulation of R_C and R_{jun} by V_{TG}. The strong modulation can also be seen in the simulation results from Figure 5c,e. Moreover, the simulated R_{ci} remains almost unchanged as depicted in Figure 5f due to the heavy n-doping effect of Sb, which is also in good agreement with our experimental results. For the Ti-contacted device, however, the simulated $2R_C$ remains constant with varied V_{TG} attributed to weak tunability of R_{jun} and R_{ci} (Figure S11), due to strong FLP. We performed further TCAD simulation to investigate how the transfer length (L_T) and junction length (L_{jun}) affect resistance components of the devices, as presented in Figures S12 and S13 (Supporting Information). When L_T increases up to 50 nm, R_{jun} of the device slightly decreases, while R_{jun} remains almost unchanged when L_T is greater than 50 nm. Thus, we believe that a further increase in L_T does not modulate the R_{jun} significantly, as depicted in Figure S12. Meanwhile, we found that increased L_{jun} results in a significant increase in R_{jun}, while R_{ci} remains almost constant regardless of L_{jun}, as shown in Figure S13 (Supporting Information). Here, L_{jun} is much more dominant in modulating R_{jun} than L_T when comparing Figures S12 and S13 (Supporting Information), suggesting L_{jun} is a key parameter for understanding the contact properties of 2D devices. Consequently, the TCAD simulations further demonstrate the origin of distinctive gate-dependent contact parameters between Ti and Sb contacts.

3. Conclusion

In conclusion, we conducted a comprehensive study on the electrical properties of MoS_2 devices contacted with semimetal (Sb) and normal metal (Ti) electrodes as a function of V_{TG} and V_{BG}. The Sb-contacted FETs revealed not only the negligible Schottky barrier but also a new insight on the role of DG structure to modulate R_C, which has not been reported in previous reports. The DG structure combining with semimetal contacts revealed the strong dependence of R_C on V_{TG}-when compared to the devices with normal metallic contacts. We utilized a new model that considers R_{jun} component to the total R_C, which shows that the weak FLP nature of semimetals modulates R_{jun} and is responsible for the significantly modulated R_C by V_{TG}. In contrast, the strong FLP in Ti-contacted devices limits the top gate-tunability of R_{jun}, resulting in unchanged R_C. TCAD simulations provided further confirmation of the contribution of V_{TG} to R_{jun} and the overall R_C improvement of Sb-contacted MoS_2 devices. The FLP-free Sb contact in DG device architecture has a significant advantage in the effective gate control of R_C, which can help achieve high-performance 2D FETs.

4. Experimental Section

Device Fabrication Process: The 2D materials (hBN and MoS_2) were mechanically exfoliated using the scotch-tape method before being transferred onto a degenerately p-doped Si wafer covered by 285 nm of thermally grown SiO_2, which is served as a global gate dielectric. The thickness of MoS_2 flakes (<5 nm) was identified by optical contrast. PMMA A6 resist was spin-coated to form a mask, followed by the electron beam lithography (EBL) process for device patterning. Subsequently, Sb/Au (Ti/Au) metal contacts with a thickness of 5/20 (5/20) nm were directly deposited with an e-beam evaporator at a vacuum pressure of 5×10^{-7} Torr. The top dielectric was formed by covering the whole structure with hBN flake (≈50 nm) via a dry pick-up and transfer process. The top gate electrode was formed through EBL patterning followed by a Ti/Au (5/70) deposition process.

Device Characterization: All electrical measurements were performed using a semiconductor parameter analyzer (Agilent 4155C) connected to a vacuum probe station with pressure maintained at 20 mTorr.

TCAD Simulations: Device analysis was performed through Synopsys Sentaurus (Synopsys Inc., Mountain View, CA, USA), a 3D technology computer-aided design (TCAD) software package. To describe the energy band characteristics of MoS_2 as a channel, the room temperature effective density-of-states N_C (300 K) and N_V (300 K) of 7.947×10^{19} cm^{-3} and 9.674×10^{19} cm^{-3}, respectively, the bandgap of 1.2 eV, and dielectric constants of $\epsilon_\perp = 6.4$ and $\epsilon_\parallel = 15.1$ were used.[37] The work function of 4.4 eV was used for both Sb and Ti metals, and SBH = 0 eV was realized at the interface between MoS_2 and Sb due to its FLP-free nature. In addition, the Sze model among the FLP models was used to describe the interface characteristics of MoS_2 and Ti. The density of interface states per unit energy (N_I) of 8.5×10^{12} cm^{-2} eV^{-1}, their extent into the semiconductor (d) of 2×10^{-7} cm, and charge neutrality level (E_{CNL}) of 5.00 eV were used to implement Schottky barrier height of 0.2 eV.

© 2023 The Authors. Advanced Science published by Wiley-VCH GmbH

21983844, 0, Downloaded from https://onlinelibrary.wiley.com/doi/10.1002/advs.202301400 by Sungkyunkwan University, Wiley Online Library on [26/06/2023]. See the Terms and Conditions (https://onlinelibrary.wiley.com/terms-and-conditions) on Wiley Online Library for rules of use; OA articles are governed by the applicable Creative Commons License

Supporting Information

Supporting Information is available from the Wiley Online Library or from the author.

Acknowledgements

This work was supported by the Global Research Laboratory (GRL) Program (2016K1A1A2912707), and the Basic Science Research Program (2021R1A2C2010869, 2022R1C1C2005607), funded by the National Research Foundation of Korea (NRF). It was also partially supported by the Ministry of Trade, Industry and Energy (20022369).

Conflict of Interest

The authors declare no conflict of interest.

Data Availability Statement

The data that support the findings of this study are available from the corresponding author upon reasonable request.

Keywords

2D semiconductors, contact resistance, dual-gate, Fermi level pinning-free, four-point-probe measurements, junction resistance, semimetal

Received: March 25, 2023
Revised: April 23, 2023
Published online:

[1] L. Wang, P. Y. Huang, Q. Gao, Y. Gao, H. Tran, T. Taniguchi, K. Watanabe, L. M. Campos, D. A. Muller, J. Guo, P. Kim, J. Hone, K. L. Shepard, C. R. Dean, *Science* **2013**, *342*, 614.
[2] T. D. Ngo, Z. Yang, M. Lee, F. Ali, I. Moon, D. G. Kim, T. Taniguchi, K. Watanabe, K.-Y. Lee, W. J. Yoo, *Adv. Electron. Mater.* **2021**, *7*, 2001212.
[3] Y. Liu, J. Guo, E. Zhu, L. Liao, S.-J. Lee, M. Ding, I. Shakir, V. Gambin, Y. Huang, X. Duan, *Nature* **2018**, *557*, 696.
[4] Y. Jung, M. S. Choi, A. Nipane, A. Borah, B. Kim, A. Zangiabadi, T. Taniguchi, K. Watanabe, W. J. Yoo, J. Hone, J. T. Teherani, *Nat. Electron.* **2019**, *2*, 187.
[5] Z. Yang, C. Kim, K. Y. Lee, M. Lee, S. Appalakondaiah, C.-H. Ra, K. Watanabe, T. Taniguchi, K. Cho, E. Hwang, J. Hone, W. J. Yoo, *Adv. Mater.* **2019**, *31*, 1808231.
[6] T. D. Ngo, M. S. Choi, M. Lee, F. Ali, Y. Hassan, N. Ali, S. Liu, C. Lee, J. Hone, W. J. Yoo, *Adv. Sci.* **2022**, *9*, 2202465.
[7] S. Cho, S. Kim, J. H. Kim, J. Zhao, J. Seok, D. H. Keum, J. Baik, D.-H. Choe, K. J. Chang, K. Suenaga, S. W. Kim, Y. H. Lee, H. Yang, *Science* **2015**, *349*, 625.
[8] P.-C. Shen, C. Su, Y. Lin, A.-S. Chou, C.-C. Cheng, J.-H. Park, M.-H. Chiu, A.-Y. Lu, H.-L. Tang, M. M. Tavakoli, G. Pitner, X. Ji, Z. Cai, N. Mao, J. Wang, V. Tung, J. Li, J. Bokor, A. Zettl, C.-I. Wu, T. Palacios, L.-J. Li, J. Kong, *Nature* **2021**, *593*, 211.
[9] A.-S. Chou, T. Wu, C.-C. Cheng, S.-S. Zhan, I.-C. Ni, S.-Y. Wang, Y.-C. Chang, S.-L. Liew, E. Chen, W.-H. Chang, C.-I. Wu, J. Cai, H.-S. P. Wong, H. Wang, in Proc. 2021 IEEE Int. Electron Devices Meeting (IEDM), IEEE, San Francisco, CA, USA **2021**, pp. 7.2.1-7.2.4.
[10] K. P. O'Brien, C. J. Dorow, A. Penumatcha, K. Maxey, S. Lee, C. H. Naylor, A. Hsiao, B. Holybee, C. Rogan, D. Adams, T. Tronic, S. Ma, A. Oni, A. Sen Gupta, R. Bristol, S. Clendenning, M. Metz, U. Avci, in Proc. 2021 IEEE Int. Electron Devices Meeting (IEDM), IEEE, San Francisco, CA, USA **2021**, pp. 7.1.1-7.1.4.
[11] Y. Wan, E. Li, Z. Yu, J.-K. Huang, M.-Y. Li, A.-S. Chou, Y.-T. Lee, C.-J. Lee, H.-C. Hsu, Q. Zhan, A. Aljarb, J.-H. Fu, S.-P. Chiu, X. Wang, J.-J. Lin, Y.-P. Chiu, W.-H. Chang, H. Wang, Y. Shi, N. Lin, Y. Cheng, V. Tung, L.-J. Li, *Nat. Commun.* **2022**, *13*, 4149.
[12] W. Li, D. Fan, L. Shao, F. Huang, L. Liang, T. Li, Y. Xu, X. Tu, P. Wang, Z. Yu, Y. Shi, H. Qiu, X. Wang, in Proc. 2021 IEEE Int. Electron Devices Meeting (IEDM), IEEE, San Francisco, CA, USA **2021**, pp. 37.3.1-37.3.4.
[13] Y. Cho, G. R. Schleder, D. T. Larson, E. Brutschea, K.-E. Byun, H. Park, P. Kim, E. Kaxiras, *Nano Lett.* **2022**, *23*, 9700.
[14] J. Lin, S. J. Koester, *IEEE Electron Device Lett.* **2022**, *43*, 639.
[15] A. Kumar, K. Schauble, K. M. Neilson, A. Tang, P. Ramesh, H.-S. P. Wong, E. Pop, K. Saraswat, in Proc. 2021 IEEE Int. Electron Devices Meeting (IEDM), IEEE, San Francisco, CA, USA **2021**, pp. 7.3.1-7.3.4.
[16] Y. Shen, Z. Dong, Y. Sun, H. Guo, F. Wu, X. Li, J. Tang, J. Liu, X. Wu, H. Tian, T.-L. Ren, *Adv. Mater.* **2022**, 2201916.
[17] H. C. P. Movva, A. Rai, S. Kang, K. Kim, B. Fallahazad, T. Taniguchi, K. Watanabe, E. Tutuc, S. K. Banerjee, *ACS Nano* **2015**, *9*, 10402.
[18] T. Wei, Z. Han, X. Zhong, Q. Xiao, T. Liu, D. Xiang, *iScience* **2022**, *10*, 105160.
[19] M. A. Rodder, A. Dodapalapur, *IEEE Trans. Electron Devices* **2019**, *66*, 4468.
[20] Z. Sun, C.-S. Pang, P. Wu, T. Y. T. Hung, M.-Y. Li, S. L. Liew, C.-C. Cheng, H. Wang, H.-S. P. Wong, L.-J. Li, I. Radu, Z. Chen, J. Appenzeller, *ACS Nano* **2022**, *16*, 14942.
[21] J. Tang, Q. Wang, Z. Wei, C. Shen, X. Lu, S. Wang, Y. Zhao, J. Liu, N. Li, Y. Chu, J. Tian, F. Wu, W. Yang, C. He, R. Yang, D. Shi, K. Watanabe, T. Taniguchi, G. Zhang, *Adv. Electron. Mater.* **2020**, *6*, 2000550.
[22] X. Huang, C. Liu, S. Zeng, Z. Tang, S. Wang, X. Chen, D. W. Zhang, P. Zhou, *Adv. Mater.* **2021**, *33*, 2102201.
[23] X. Huang, C. Liu, Z. Tang, S. Zeng, L. Liu, X. Hou, H. Chen, J. Li, Y.-G. Jiang, D. W. Zhang, P. Zhou, in Proc. 2021 IEEE Int. Electron Devices Meeting (IEDM), IEEE, San Francisco, CA, USA **2020**, pp. 12.1.1-12.1.4
[24] M. Liu, J. Niu, G. Yang, K. Chen, W. Lu, F. Liao, C. Lu, N. Lu, L. Li, *Adv. Electron. Mater.* **2022**, *9*, 2200722.
[25] C. J. Dorow, A. Penumatcha, A. Kitamura, C. Rogan, K. P. O'Brien, S. Lee, R. Ramamurthy, C.-Y. Cheng, K. Maxey, T. Zhong, T. Tronic, B. Holybee, J. Richards, A. Oni, C.-C. Lin, C. H. Naylor, N. Arefin, M. Metz, R. Bristol, S. B. Clendenning, U. Avci, in Proc. 2022 IEEE Int. Electron Devices Meeting (IEDM), IEEE, San Francisco, CA, USA **2022**, pp. 7.5.1–7.5.4.
[26] C. Kim, I. Moon, D. Lee, M. S. Choi, F. Ahmed, S. Nam, Y. Cho, H. J. Shin, S. Park, W. J. Yoo, *ACS Nano* **2017**, *11*, 1588.
[27] T. D. Ngo, M. Lee, Z. Yang, F. Ali, I. Moon, W. J. Yoo, *Adv. Electron. Mater.* **2020**, *6*, 2000616.
[28] A. Allain, J. Kang, K. Banerjee, A. Kis, *Nat. Mater.* **2015**, *14*, 1195.
[29] a) E. Ber, R. W. Grady, E. Pop, E. Yalon, (Preprint) arXiv:2110.02563, v1, submitted: Oct **2021**; b) E. Ber, R. W. Grady, E. Pop, E. Yalon, *Adv. Electron. Mater.* **2023**, https://doi.org/10.1002/aelm.202201342.
[30] S. Venica, F. Driussi, A. Gahoi, P. Palestri, M. C. Lemme, L. Selmi, *IEEE Trans. Electron Devices* **2018**, *65*, 1589.
[31] A. Gahoi, S. Kataria, F. Driussi, S. Venica, H. Pandey, D. Esseni, L. Selmi, M. C. Lemme, *Adv. Electron. Mater.* **2020**, *6*, 2000386.
[32] L. Kong, X. Zhang, Q. Tao, M. Zhang, W. Dang, Z. Li, L. Feng, L. Liao, X. Duan, Y. Liu, *Nat. Commun.* **2020**, *11*, 1866.
[33] G. Zhang, G. Lu, X. Li, Z. Mei, L. Liang, S. Fan, Q. Li, Y. Wei, *ACS Nano* **2023**, *17*, 4564.
[34] D. R. Lide, *CRC Handbook of Chemistry and Physics*, CRC Press, Boca Raton, FL **2001**.
[35] Y. Yang, N. Huo, J. Li, *J. Mater. Chem. C* **2017**, *5*, 7051.
[36] P. Wen, L. Zhang, W. Gao, Q. Yue, H. Wang, Y. Huang, J. Wu, H. Yu, H. Chen, N. Huo, J. Li, *Adv. Electron. Mater.* **2022**, *8*, 2101144.
[37] A. Laturia, M. L. Van de Put, W. G. Vandenberghe, *npj 2D Mater. Appl.* **2018**, *2*, 6.

© 2023 The Authors. Advanced Science published by Wiley-VCH GmbH

21983844, 0, Downloaded from https://onlinelibrary.wiley.com/doi/10.1002/advs.202301400 by Sungkyunkwan University, Wiley Online Library on [26/06/2023]. See the Terms and Conditions (https://onlinelibrary.wiley.com/terms-and-conditions) on Wiley Online Library for rules of use; OA articles are governed by the applicable Creative Commons License